Particle Reduced, Efficient Gasoline Engines

EUROPEAN COMMISSION
Horizon 2020 | GV-2-2016 | Technologies for low emission light duty powertrains
GA # 723954

Deliverable No.	PaREGEn D1.3	
Deliverable Title	Report on spray and spray/wall interaction CFD model validation.	
Deliverable Date	2018-03-31	
Deliverable Type	REPORT	
Dissemination level	Public (PU)	
Written By	Nicolò Frapolli (ETH Zurich)	2018-03-17
Checked by	Andreas Manz (Bosch) Yuri M. Wright (ETH Zurich) Bastian Morcinkowski (FEV)	2018-03-29 2018-03-27 2018-03-26
Approved by	Andreas Manz (Bosch) Simon Edwards (RIC) - Coordinator	2018-03-31 2018-03-31
Status	Final	2018-04-23

Summary

With the objective of achieving an increased efficiency of at least 15%, while at the same time complying with the Euro 6c regulations limiting the emitted particles number (PN) per kilometre to 6 x 10^{11}, the PaREGEn project aims at developing the next generation of gasoline direct injection (GDI) engines for medium to premium size passenger cars. This limitation in particulate emissions is especially challenging in gasoline direct injection engines due to the inhomogeneities in the air-fuel mixture. In particular, these inhomogeneities arise near to fuel wall-films, on the piston or on the cylinder wall, due to fuel deposition and subsequent evaporation. As a consequence, in these zones of the combustion chamber, the formation of polycyclic aromatic hydrocarbons (PAH) and soot during combustion is likely. In this context, one objective of the PaREGEn project is to improve the understanding of Cause and Effect Relationship (CER) of particle formation during the in-cylinder processes related to gasoline direct injection combustion. This is achieved by advanced optical diagnostics, in-cylinder measurements, as well as by numerical simulations through advanced models and powerful calculators. In particular, in Task 1.4 of the PaREGEn project, models for spray development as well as for spray/wall interaction are assessed by numerical simulations in three different main set-ups. Each set-up is designed in order to separate different physical aspects and is simulated by increasing the complexity and the physical insights: from the simple spray morphology, all the way to spray development and wall-film formation in a fully developed flow in a real engine.

The first assessment is executed in a constant-volume chamber, where spray development and dynamics are simulated and compared to the corresponding measurement performed at Bosch. Next, both spray development and spray/wall interaction, leading to the formation of a liquid film, are simulated in an optical accessible flow channel, whose corresponding experiments are conducted at the University of Duisburg-Essen (UDE). In this case, spray morphology as well as wall-film formation can be assessed by measurements of the spray penetration and two-dimensionally resolved wall-film deposition on the wall on the opposite side to the injector. Additionally, fuel evaporation is also visualized in order to highlight inhomogeneities in the mixture due to wall-film formation. Finally, spray impingement and subsequent liquid film formation are simulated and compared to the experiments in a single cylinder optical engine. Experiments are performed at Bosch in an optically accessible engine in two different configurations: the first with a still-standing piston, the second-one at motored conditions. The same two configurations are also reproduced by numerical simulations.

In order to first evaluate the capabilities and the limits of the different numerical simulations models in reproducing the main physical insight of a typical gasoline engine spray, the first simulations are conducted in a constant volume chamber as in the experiments performed at Bosch. In this case, the project injector is employed and tested with gasoline at different injection pressures, ambient pressures, and fuel injection temperatures. This leads to different physical aspects, which span from a typical spray evolution at ambient conditions (1 bar) to the flash-boiling condition and/or spray collapse in case of throttled operation (pressure well below ambient conditions). Simulations are carried out employing Large Eddy Simulations (LES) models for the evolution of the flow field, while the liquid phase of the spray is treated by a Lagrangian-Eulerian approach, enabling an efficient multiphase treatment typical for spray simulations. Due to the employment of a Lagrangian approach for the liquid phase, many assumptions and simplifications were needed. In particular, neither the exact nozzle geometry nor the exact flow field development inside the nozzle are simulated accurately. This leads to great efforts in tuning and identifying appropriate sub-models and corresponding parameters for the nozzle, the atomization and the droplet break-up. It was found that the following models were bests suited for gasoline spray injection at different operating condition in a Lagrangian-Eulerian framework: first, the injector is modelled using the Max Planck Institute modified nozzle model (MPI2), which allows to specify a discharge coefficient as well as the contraction ratio similar as in the real nozzle. Next, the atomization process is modelled with the Reitz-Diwakar model, with the drawback of specifying spray semi-cone angle, while for the break-up dynamics the KHRT (Kelvin-Helmholtz Rayleigh-Taylor) model is employed. The most challenging condition to simulate was the one for when flash-boiling

and subsequent spray collapse occurred, since most of the models employed for spray simulations are calibrated and employed for Diesel spray injection or conventional gasoline injection. What enable the simulation of flash-boiling in gasoline spray direct-injection is the combination of the Reitz-Diwakar model together with the KHRT model. In addition to the sub-model's key constants sensitivity study, a grid sensitivity study was carried out in the constant volume spray chamber set-up in order to evaluate possibilities of grid relaxation toward grid size requirements in the engine set-up. For this last task, in fact, the grid must be kept as coarse as 0.5 mm, due to computational requirements reasons. This has led to a spray model calibration working also for grids of the order of δ = 0.5 mm. The simulations carried out in this set-up were validated by comparisons of spray vapour penetration length following ECN (Engine Combustion Network) criteria, as well as by spray morphology comparison; in this last case, the fuel concentration is compared with shadow images produced by the experiments at different times after injection.

Spray evolution and wall-film formation in the optical engine geometry is also reported here by showing preliminary results at fixed piston positions. The spray evolution is very similar to the one in the spray chamber at constant volume. This set-up is, therefore, well suited to evaluate wall-film models without the influence of complex flow motions due to the high-speed piston and valve motions. Wall-film results from numerical simulations are compared to the Laser-Induced Fluorescence (LIF) results acquired at Bosch. The model employed for droplets/wall interaction is the Bai model, while wall liquid film is simulated employing the Bai and Gosman model.

The experience gained by these simulations will be used for wall-film formation at relevant conditions involving intake and exhaust processes, including valves and piston motion and significant turbulence levels. In parallel, the same process will be also simulated in the flow channel. This will be particularly useful for the future next steps of the project, allowing analysis and deeper insight into the fuel evaporation from a wall-film after flame propagation. In turn, this will provide useful insights into the CER of soot formation.

The results reported here highlight the good prediction capabilities of the numerical simulations in reproducing the spray development for both conventional gasoline injection as well as for flash-boiling and spray collapse, in terms of both vapour penetration length and spray morphology. The prediction capabilities of the spray are further extended for the simulation of wall-film formation, and in this case, the results compare satisfactorily with the experimental measurements.

All information and measurements reported here about experimental results are collected from Sub-task 1.4.1.2. In particular, the spray chamber measurements are used to validate spray development and morphology, while optical engine wall-film measurements are used as validation of the wall-film models in the present report. Flow channel measurements will be employed for further validating the numerical simulations and, in particular, for their extension to combustion and soot simulation. The results obtained here may be used in Sub-task 1.4.4 to optimize the combustion and soot models. Moreover, detailed information extrapolated from the 3D-CFD simulations may serve to improve the Virtual Gasoline Particle Sensor of Sub-task 1.5.2.

Contents

Figures

Tables

Introduction

Ever more restrictive regulations on particulate emissions, which for the Euro 6c regulation are fixed to a particle number of 6 x 10^{11} per kilometre, combined with the necessity to increase fuel saving thus to improve engine efficiency, lead to more efforts in understanding the particulate formation during combustion. In the particular case of this part of the PaREGEn project, Cause and Effect Relationship (CER) of particle formation during the in-cylinder processes related to gasoline direct injection (GDI) combustion is investigated through numerical simulations, supported by a validation with advanced experimental techniques for measuring spray vapour penetration, spray morphology and wall-film formation.

In order to get a deeper understanding of the CER of particle formation, Large Eddy Simulations in combination with a Lagrangian treatment of the liquid phase are carried out, in combination with different sub-models, in three different set-ups: a constant volume spray chamber, where the spray evolution and morphology is evaluated, a flow channel, where both spray and spray impingement on the wall are evaluated, and an optical engine, where spray/wall interaction and subsequent wall-film formation are evaluated for both a standing piston and motored conditions.

Due to the employment of a Lagrangian approach to treat the two-phase flow – which represents the liquid phase by means of discrete droplet parcels – many assumptions and simplifications were needed since the flow field development inside the nozzle is not resolved. This leads to significant efforts with respect to the identification of the most appropriate sub-models, parameterization of their respective model constants for the nozzle, the atomization and the droplet break-up process. It was found that the following models were best suited for gasoline spray injection at different operating condition in a Lagrangian-Eulerian framework: first, the injector is modelled using the Max Planck Institute modified nozzle model (MPI2), which allows a discharge coefficient as well as the contraction ratio to be specified, similarly to as in real nozzles. Next, the atomization process is modelled using the Reitz-Diwakar model. Finally, the break-up dynamics are modelled with the KHRT (Kelvin-Helmholtz Rayleigh-Taylor) model. The Reitz-Diwakar model has the drawback of specifying spray semi-cone angle, but it is employed here in combination with the KHRT model because of the excellent results that are obtained.

The capabilities and limits of the numerical simulations in reproducing the main physical aspects of a typical gasoline engine spray are initially evaluated in a constant volume spray set-up. In this set-up, the PaREGEn project injector is employed and tested with gasoline at different injection pressures, ambient pressures, and fuel injection temperatures. The corresponding spray physics span from typical spray evolutions at ambient conditions (1 bar) to flash-boiling conditions and/or spray collapse in case of throttled conditions (0.4 bar in this specific case with an injection fuel temperature of 80° C). The latter operating condition is particularly challenging to simulate, since most of the models employed for spray simulation are calibrated and employed mostly for Diesel spray injection or conventional gasoline injection at ambient conditions. What enables the simulation of flash-boiling in gasoline spray direct-injection is the combination of the Reitz-Diwakar model together with the KHRT model. These models, in fact, enables one to mimic the break-up process appearing at the nozzle exit during flash-boiling, i.e. the formation of a large number of droplets considerably smaller than the nozzle exit area (Sher, Bar-Kohany, & Rashkovan, 2008). At the same time, specifying the semi-cone angle allows for adjustment of the widening of the spray when the ambient pressure is drastically reduced. This leads to a semi-cone angle of around 41° under flash-boiling conditions due to the low ambient pressure, in contrast to the 17° typical for Diesel and gasoline spray injection at high and ambient pressures respectively.

This report also contains results related to the spray evolution and wall-film formation in the optical engine geometry, in particular for the standing piston case. The spray evolution is very similar to the one in the spray chamber at constant volume. This set-up is then well suited to evaluate wall-film models without the influence of complex flow motion due to the piston and valve motions at high speed. Wall-film results from numerical simulations are compared to Laser-Induced Fluorescence (LIF) data acquired at Bosch. As a next

step, wall-film formation will be evaluated in the case of intake and exhaust processes, including valves and piston motion.

In parallel to wall-film formation in the engine, the same process will be also evaluated in the flow channel. This will be particularly useful for the future next steps of the project. Validation of the wall-film in this set-up, in fact, will allow, in the future when combustion will be simulated in the channel, the analysis and deeper insight into the fuel evaporation from wall-film after flame propagation.

1 Methods and results

In the first part of this section, the basic equations, models and sub-models employed to simulate liquid spray evolution are described, first for the gaseous phase, by presenting an overview over the Large Eddy Simulations and related sub-models, next for the liquid phase, by presenting the basic models and sub-models for the Lagrangian treatment. In the second part of this section, the numerical set-ups employed to simulate the constant volume chamber and the optical engine experiments are briefly described. In the last part of the section, the relevant results of the numerical simulations are presented.

1.1 Governing equations

The governing equations for the numerical simulations of spray evolution employing an Eulerian-Lagrangian approach are briefly reported in the following. The software used to compute all numerical simulations is Star-CD. It has to be noted, that no new models have been developed here; all the models employed in this report were already implemented in Star-CD, and all efforts of this work were concentrated in looking for the best combination of models and sub-models together with the corresponding optimal parameters.

1.1.1 Large-eddy simulations formulation

The Large Eddy Simulation (LES) equations, employed for the simulation of the gaseous phase, are derived from the Navier-Stokes equations by applying a spatial filter in such a way as to resolve only the large-scale turbulent motions, while the smaller scales are modelled by suitable sub-models (Germano, 1992). The resulting LES equations for compressible flows can be written as

$$\frac{\partial \bar{\rho}}{\partial t} + \frac{\partial \bar{\rho}\tilde{u}_i}{\partial x_i} = 0, \tag{1}$$

$$\frac{\partial \bar{\rho}\tilde{u}_i}{\partial t} + \frac{\partial \bar{\rho}\tilde{u}_i\tilde{u}_j}{\partial x_j} + \frac{\partial \bar{p}}{\partial x_i} = -\frac{\partial \bar{\rho}\tau_{ij}^r}{\partial x_j} + \frac{\partial \bar{\sigma}_{ij}}{\partial x_j}, \tag{2}$$

where Eq. 1 and Eq. 2 are the conservation of mass and momentum respectively, $\bar{\rho}$ is the mean density, $\tilde{u}$ is the Favre averaged velocity vector, $\bar{p}$ is the pressure, $\bar{\sigma}_{ij}$ is the shear stress tensor, given by

$$\sigma_{ij} = 2\mu(T)S_{ij} - \frac{2}{3}\mu(T)\delta_{ij}S_{kk}, \tag{3}$$

where $\mu(T)$ is the dynamic viscosity, T the temperature and $S_{ij} = \frac{1}{2}\left(\frac{\partial u_i}{\partial x_j} + \frac{\partial u_j}{\partial x_i}\right)$ the rate of strain tensor. Finally, $\tau_{ij}^r = \widetilde{u_i u_j} - \tilde{u}_i\tilde{u}_j$ is the sub-grid stress-tensor for the Favre-averaged momentum field. In order to model sub-grid scales, in this work the sub-grid scales tensor is modelled via an eddy-viscosity type closure, which assumes a linear relationship between the sub-grid stress-tensor and the rate of strain tensor:

$$\tau_{ij}^r = -\mu_t\tilde{S}_{ij} + \frac{1}{3}\bar{\rho}\widetilde{u_k u_k}, \tag{4}$$

where μ_t is the turbulent viscosity, which depends on the chosen sub-model. In this work, the $\kappa - l$ model is employed, due to its simplicity and reduced computational cost (Horiuti, 1992). The turbulent viscosity can then be written as:

$$\mu_t = C_2\bar{\rho}\Delta\kappa_{SGS}^{0.5}, \tag{5}$$

where C_2 is a model constant set to 0.05, Δ is the cell characteristic size and κ_{SGS} is the turbulent kinetic energy, for which an equation of the form

$$\frac{\partial \bar{\rho}\kappa_{SGS}}{\partial t} + \frac{\partial \bar{\rho}\tilde{u}_j\kappa_{SGS}}{\partial x_j} = -\overline{\sigma_{ij}}\,\bar{S}_{ij} - C_1\bar{\rho}\frac{\kappa_{SGS}^{\frac{2}{3}}}{\Delta} + \frac{\partial}{\partial x_j}\left[C_2\bar{\rho}\Delta\kappa_{SGS}^{0.5}\frac{\partial \kappa_{SGS}}{\partial x_j}\right], \tag{6}$$

is derived, and where C_1 is a second model constant set to 0.6.

In order to simulate compressible flow, conservation of energy has to be taken into account. To do so, the chemico-thermal static enthalpy equation of the form

$$\frac{\partial \rho h}{\partial t} + \frac{\partial}{\partial x_j}\left(\rho h u_j + F_{h,j}\right) = \frac{\partial p}{\partial t} + u_j\frac{\partial p}{\partial x_j} + \tau_{ij}\frac{\partial u_i}{\partial x_j} + s_h, \tag{7}$$

is solved in its Favre-averaged filtered version with the sub-models of the same type as for the momentum equation. Here, the static enthalpy $h \equiv \bar{c}_p T - c_p^0 T_0 + \sum Y_m H_m$, where $\bar{c}_p$ is the mean constant-pressure specific heat at temperature T, c_p^0 is the corresponding reference value at reference temperature T_0, Y_m is the mass fraction of specie m, and H_m is the heat of formation of species m.

1.1.1.1 Discretization and solution algorithm

Spatial discretization is carried out by a finite volume formulation, while the Pressure Implicit with Splitting of Operators (PISO) algorithm for the pressure solution is employed together with a first-order implicit Euler scheme for time discretization. Mass and momentum equations are differentiated by a central-differences scheme, while the energy conservation equation by the Monotone Advection and Reconstruction Scheme (MARS). For more information about the discretization procedure the reader is referred to the Star-CD methodology (Siemens PLM Software, 2017).

1.1.2 Lagrangian treatment

The liquid phase dispersed in the gaseous phase, arising during liquid spray injection, is modelled here with a Lagrangian approach. As a consequence, a lot of assumptions and simplifications are carried out for what concerns the liquid phase. In particular, neither the exact nozzle geometry nor the exact flow field development inside the nozzle are simulated accurately, since the droplets are simulated only from the moment they exit the nozzle. However, this approach allows to simulate quite accurately the statistically relevant quantities related to a dense spray while at the same keeping the computational cost low. In the Lagrangian approach considered here, the injected liquid is divided into elements for which mass, momentum and energy conservation equations are solved (Bracco, 1985). Since the number of elements may be large for a realistic gasoline direct injection spray, a statistical approach is employed here: only a limited number of computational parcels is used, each one representing a limited number of elements (droplets) having the same properties.

1.1.2.1 Basic conservation equations

Every parcel representing a group of droplets obeys the conservation of mass, momentum and energy equations, given respectively by

$$\frac{dm_d}{dt} = -A_s F_m, \tag{8}$$

$$m_d\frac{d\boldsymbol{u}_d}{dt} = \boldsymbol{F}_{dr} + \boldsymbol{F}_p + \boldsymbol{F}_{am} + \boldsymbol{F}_b, \tag{9}$$

$$m_d c_{p,d} \frac{dT_d}{dt} = -A_s \dot{q}_d'' + h_{fg} \frac{dm_d}{dt}, \tag{10}$$

where m_d is the droplet mass, A_s is the droplet surface area, F_m is the mass transfer rate per unit area, $\boldsymbol{u}_d$ is the droplet velocity vector, $\boldsymbol{F}_{dr}$ is the drag force, $\boldsymbol{F}_p$ is the pressure force, $\boldsymbol{F}_{am}$ is the "virtual mass" force, $\boldsymbol{F}_b$ is the general body force, $c_{p,d}$ the droplet specific heat, T_d the droplet temperature, $\dot{q}_d''$ the surface heat flux and h_{fg} the latent heat of phase change.

1.1.2.2 Nozzle model

The first part of the Lagrangian liquid phase modelling, consists in modelling injection, which is performed with an injector model. Here, an MPI2 model for the injector is employed (Obermeier, 1991). This type of model, is particularly well suited to simulate gasoline direct injection when flash-boiling occurs, since in addition to the discharge coefficient, a contraction ratio of the nozzle diameter can also be taken into account. This helps in reducing the inlet droplet diameter, similar to the processes appearing in flash-boiling. Moreover, this model is theoretically able to recognize the formation of cavitation at the entrance or in the nozzle duct.

1.1.2.3 Atomization model

Together with the nozzle model, the atomization model plays an important role in the inlet condition of the droplets at the nozzle exit. Here, the Reitz-Diwakar atomization model is employed (Reitz & Diwakar, 1986). Within the framework of this model, the spray angle is an input parameter, while the initial velocity distribution is computed according to the velocity resulting from the nozzle model, with a random initial direction computed within the specified cone angle range. The atomization model has a strict dependency with the break-up model which is described in next sub-section.

1.1.2.4 Break-up model

Break-up models are required in order to simulate droplet instability and subsequent break-up into smaller droplets. The break-up model employed here is the Kelvin-Helmholtz Rayleigh-Taylor model (KHRT) (Patterson & Reitz, 1998). The general formulation for break-up models and thus for droplet decay into smaller droplets is of the form:

$$\frac{dD_d}{dt} = -\frac{\left(D_d - D_{d,stable}\right)}{\tau_b}, \tag{11}$$

where D_d is the actual droplet diameter, $D_{d,stable}$ is an estimate of the stable droplet diameter and τ_b is the characteristic time scale of the droplet break-up. A break-up model is designed in such a way as to find $D_{d,stable}$ and τ_b. In the KHRT model, the Kelvin-Helmholtz aerodynamics instabilities and Rayleigh-Taylor instabilities arising due to droplet deceleration are taken into account and estimated. The two physical processes compete with each other, and the fastest determines the onset of break-up. In the case of the KH instability, the stable diameter and characteristic time are given by

$$D_{KH} = 2B_0 \Lambda_{KH}, \tag{12}$$

$$\tau_{KH} = \frac{3.726 B_1 \mathrm{D}_d}{2\Lambda_{KH}\Omega_{KH}}, \tag{13}$$

with B_0 and B_1 being model constants which depend on the operating conditions, Λ_{KH} the wavelength of the growing unstable surface wave, and Ω_{KH} the growing rate of the fastest growing wave. For the case of the RT model, the stable diameter and characteristic times are given by

$$D_{RT} = C_3 \Lambda_{RT}, \tag{14}$$

$$\tau_{RT} = \frac{C_\tau}{\omega_{RT}}, \tag{15}$$

where C_3 and C_τ are model constants, Λ_{RT} is the RT fastest growing wave wavelength, and $\omega_{RT} = \omega(2\pi/\Lambda_{RT})$ is the maximum growth rate.

1.1.2.5 Collision model

The collision model employed within the framework of Star-CD is the O'Rourke model (O'Rourke, 1981), which distinguish mainly three types of interactions: coalescence, separation and bouncing. While the separation and bouncing mechanisms involve only a momentum transfer, coalescence needs to take into account also mass and energy transfer.

1.1.2.6 Droplet-wall interaction model

The model employed for droplet impingement is the Bai's model (Bai & Gosman, Development of methodology for spray impingement simulation, 1995), which takes into account a number of parameters associated with the droplet and the wall, such as droplet velocity and angle with respect to the wall, droplet size and temperature-dependent thermo-physical properties, wall temperature and roughness, wetted or dry wall, liquid-film thickness, as well as near wall gas conditions. The model accounts for three wall temperature regimes, each-one distinguishing between a dry or wetted wall, while droplet to wall-film transition is governed by a number of criteria discussed in Section 1.1.3 below.

Two characteristics, non-dimensional numbers are used to combine a larger number of parameters into a smaller one; these numbers are the Weber number,

$$\mathrm{We} = \frac{\rho|\boldsymbol{u} - \boldsymbol{u}_d|^2 D_d}{\sigma_d}, \tag{16}$$

and the Laplace number,

$$\mathrm{La} = \frac{\rho_d \sigma_d D_d}{\mu_d^2}, \tag{17}$$

where ρ_d is the droplet density, σ_d is the surface tension of the droplet, and μ_d is the droplet viscosity. Moreover, two characteristic temperatures are also employed: the rebound temperature,

$$T_s^* = B_s T_{boiling}, \tag{18}$$

and the sliding temperature,

$$T_{LEID}^* = B_l T_{Leidenfrost}, \tag{19}$$

where B_s and B_l are the multiplying factors of the boiling and Leidenfrost temperatures respectively.

Three wall temperatures regimes are taken into account here, each-one distinguishing between a dry or wetted wall. In the following, the three regimes are briefly presented.

<u>Range 1</u>: $T_w \leq T_s^*$

In this range of temperature, a quite large number of regimes may occur. These may be: stick, in which the impinging droplet adheres to the wall in a nearly spherical form; spread: the droplet spreads forming a liquid film or merges with an already existing liquid film; rebound: the impinging droplet rebounds away from the

wall after the impact; splash: the droplet breaks-up into smaller droplets, some of which are reflected from the wall; break-up: the droplet breaks-up into smaller droplets, which are all reflected from the wall.

1. Dry wall: in case of dry wall, two regimes are taken into account: the first is the adhesion, which includes both stick and spread regimes, and which belongs to the range

$$\mathrm{We}_d \leq A\, La^{-0.18},$$

where A is a coefficient depending on surface roughness: the second is the splashing, which is set for

$$\mathrm{We}_d > A\, La^{-0.18}.$$

2. Wetted wall: in case of wetted wall, three regimes are considered. The rebound

$$\mathrm{We}_d \leq 5,$$

the spread

$$5 \leq \mathrm{We}_d \leq A_w\, La^{-0.18},$$

and the splash

$$\mathrm{We}_d > A_w\, La^{-0.18},$$

where A_w is an empirical coefficient set to 1320.

<u>Range 2</u>: $T_s^* < T_w \leq T_{LEID}^*$

In this range, droplet deposition cannot occur due to the presence of a vapour film. Thus, the mechanisms that may appear are distinguished as follows:

1. Rebound:

$$\mathrm{We}_d \leq We_1^T,$$

2. Break-up and rebound:

$$We_1^T \leq \mathrm{We}_d \leq We_2^T,$$

3. Break-up and spread:

$$We_2^T \leq \mathrm{We}_d \leq We_a,$$

4. Splash without deposition:

$$\mathrm{We}_d > We_a,$$

where We_1^T, We_2^T and We_a are characteristic Weber numbers.

<u>Range 3</u>: $T_w > T_{LEID}^*$

In this case, wall contact is also avoided due to the presence of a vapour film; the regimes that are taken into account are thus:

1. Spread:
$$\mathrm{We}_d \leq We_1^T,$$
2. Break-up and spread:
$$We_1^T \leq \mathrm{We}_d \leq We_a,$$
3. Splash without deposition:
$$\mathrm{We}_d > We_a.$$

1.1.3 Wall-film modelling

Wall-film modelling employs conservation equations governing liquid film dynamics, as well as a criterion to make the transition from the droplet mode to the wall-film mode. This model has been developed by Bai and Gosman in (Bai & Gosman, Mathematical modeling of wall films formed by impinging sprays, 1996). In the following, the droplet to wall-film transition criterion is presented, and is followed by the conservation equations governing the dynamic of the wall-film.

1.1.3.1 Transition criterion

Every droplet impacting on the wall obeys the criteria of the droplet-wall interaction model of Section 1.1.2.6; if the droplet is staying on the wall, then it is assumed to spread into a cylindrical form of diameter D_s. The droplet to wall-film transition criterion is based on the droplet surface coverage ratio γ_c, defined as

$$\gamma_c = \frac{\pi}{4A_c}\sum_i D_{s,i}^2 N_i, \tag{20}$$

where A_c is the area of the face of the cell in which the droplet resides, and N_i is the number of droplets in the ith parcel. The coverage ratio is continuously updated until it reaches a threshold value, which here is set to be 0.01. When the threshold value is reached, the mass of the droplets in the cell is converted in liquid film thickness and mass.

1.1.3.2 Wall-film conservation equations

The wall-film is considered to obey to the laws of conservation of mass, momentum and energy. The mass conservation equation is written as

$$\frac{\partial \rho_l}{\partial t} + \frac{\partial \rho_l u_{l,i}}{\partial x_i} = \frac{\dot{m}_{imp}}{h}, \tag{21}$$

while the momentum conservation equation is written as

$$\frac{\partial \rho_l u_{l,i}}{\partial t} + \frac{\partial \rho_l u_{l,i} u_{l,j}}{\partial x_j} + \frac{\partial p_l}{\partial x_i} = \rho_l g_i + \frac{\partial \tau_{l,ij}}{\partial x_j} + S_{i,imp}\delta(\xi - h), \tag{22}$$

and finally, the energy conservation equation is written as

$$\frac{\partial \rho_l h_l}{\partial t} + \frac{\partial \rho_l u_{l,j} h_l}{\partial x_j} = \frac{\partial}{\partial x_j}\left(\kappa_l \frac{\partial T_l}{\partial x_j}\right) + \frac{\dot{Q}_{imp}}{h}, \tag{23}$$

where pedice l refers to liquid film, ρ_l is its corresponding density, $u_{l,i}$ is the velocity vector, $\dot{m}_{imp}$ is the mass source/sink per unit area due to droplet wall impingement, h is the film thickness, p_l is the film pressure, g_i is the gravity vector, $\tau_{l,ij}$ is the stress-tensor, $S_{i,imp}$ is the momentum source corresponding to the mass source, δ is the Dirac delta function, h_l is the enthalpy of the film, T_l is its temperature, κ_l the thermal conductivity, and $\dot{Q}_{imp}$ is the heat source corresponding to the mass and momentum source.

An extension to evaporation and condensation is presented in (Sirignano, 1999) and (Torres, O'Rourke, & Amsden, 2003), while for more information about details and extensions of the model together with discretization information can be found in the Star-CD methodology guide (Siemens PLM Software, 2017).

1.2 Numerical set-up

The two main numerical set-ups are described in the following: the constant volume spray chamber and the optical engine. The flow channel set-up is not described since the simulations for this case will be run only in a next step.

1.2.1 Constant volume chamber

The first set-up employed in the simulations is the constant volume chamber, where the project injector is located at the centre of one wall. The chamber is filled with pure nitrogen, at an ambient temperature of $T_{amb} = 20°C$, and in calm conditions (no turbulence and flow at rest). For all the three cases considered here, the injection duration is set to $t_{inj} = 1.5\ ms$, and the injected fuel is a single-component surrogate for gasoline, while ambient pressure P_{amb}, injection pressure P_{inj}, and injection temperature T_{inj} are varied. The mass-flow-rate from each injector hole is estimated taking into account a discharge coefficient $c_d = 0.68$, and reads:

$$\dot{m} = \rho_f \pi \left(\frac{d}{2}\right)^2 c_d \sqrt{\frac{2\left(P_{inj} - P_{amb}\right)}{\rho_f}}. \tag{24}$$

It has to be noted that a ramp mass flow rate has been imposed in the numerical simulation in order to mimic the rate of injection of the experiments: the injection mass flow rate starts with ¾ of the nominal mass flow rate and increases reaching the nominal mass flow rate in 0.15 *ms*, and the same amount in the same duration is applied in order to decrease injection mass flow rate at the end of the injection, in such a way as to obtain a "symmetrical" injection profile over time.

The most important parameters for obtaining different operational modes, i.e. normal gasoline operation or flash-boiling conditions, are the break-up constants of the KHRT model § 1.1.2.4, and the cone angle of the spray θ in § 1.1.2.3. These parameters are reported together with the operating conditions in Table 1.

	OP1	**OP2**	**OP3**
P_{amb} [Pa]	$1.05 \cdot 10^5$	$0.4 \cdot 10^5$	$1.05 \cdot 10^5$
P_{inj} [Pa]	$2.0 \cdot 10^7$	$2.0 \cdot 10^7$	$3.5 \cdot 10^7$
T_{inj} [°C]	20	100	20
$\dot{m}$ [mg/s]	2.2009	2.2045	2.8063
θ [°]	17	41	18
B_0 [-]	0.4	0.33	0.4
B_1 [-]	40	20	40
C_3 [-]	0.6	0.033	0.6
C_τ [-]	1.0	0.3	1.0

Table 1: Operating conditions parameters of the constant volume chamber simulations.

It has to be noted, that the employment of gasoline instead of iso-octane may lead to different spray evolutions. Gasoline in fact, has a higher tendency toward flash-boiling and spray collapse at same ambient and injection conditions. This needs to be taken into account when employing gasoline in the spray simulations and then replicating the same conditions with a spray of iso-octane, as for example the wall-film simulations in the optical engine.

1.2.2 Optical engine

The second set-up employed in the simulations is the optical engine operated by and at Bosch. The technical data of the engine are reported in Table 2.

Bore	[mm]	82
Stroke	[mm]	85
Connecting rod length	[mm]	146.5
Compression ratio	[-]	10.5:1

Table 2: Optical engine data.

In Figure 1, the engine geometry is represented together with the injector location. The injector is tilted 11° toward the negative x-axis direction. Intake port is on the left while exhaust is on the right.

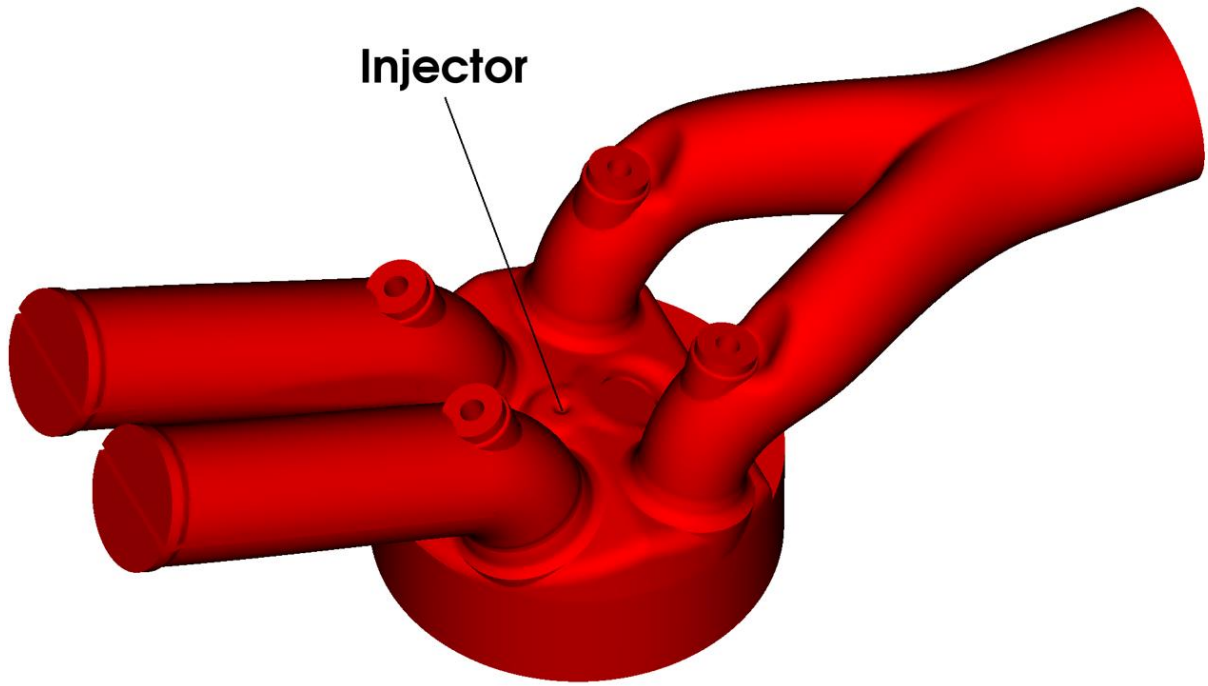

Figure 1: Engine geometry representation together with injector location.

Here, the effect of different fixed piston positions is investigated, for two different injection pressures. The data for each operating point are shown in Table 3.

	P360_35MPa	P330_35MPa	P330_35MPa	P360_20MPa	P330_20MPa	P300_20MPa
Piston position [° CA]	360	330	300	360	330	300
P_{amb} [Pa]	$1.05 \cdot 10^5$	$1.05 \cdot 10^5$	$1.05 \cdot 10^5$	$1.05 \cdot 10^5$	$1.05 \cdot 10^5$	$1.05 \cdot 10^5$
T_{amb} [°C]	20	20	20	20	20	20
P_{inj} [Pa]	$3.5 \cdot 10^7$	$3.5 \cdot 10^7$	$3.5 \cdot 10^7$	$2.0 \cdot 10^7$	$2.0 \cdot 10^7$	$2.0 \cdot 10^7$
T_{inj} [°C]	20	20	20	20	20	20
T_{wall} [°C]	20	20	20	20	20	20
$\dot{m}$ [mg/s]	2.9148	2.9148	2.9148	2.1190	2.1190	2.1190
t_{inj} [ms]	1.567	1.567	1.567	2.079	2.079	2.079

Table 3: Operating conditions parameters of the standing piston engine simulations.

Three engine piston positions have been simulated: P360, where the piston position is at Top Dead Centre, P330, where the piston position is at 30° after Top Dead Centre and P300, where the piston position is at 60° after Top Dead Centre. For all three cases, two injection pressures are used, i.e. the same as for the constant volume chamber: 20 MPa and 35 MPa. Accordingly, all model parameters and mass flow rate are the same as for the corresponding constant volume chamber operating condition (OP1 or OP3, with $P_{amb} = 1.05 \cdot 10^5$ and $T_{amb} = 20°$ C). In all the cases, the injected fuel mass is $m_{tot} = 27.4$ mg, and the injection duration is adjusted accordingly. The fuel is considered to be iso-octane, while the gas engine is air (21% oxygen, 79% nitrogen).

For more information about the two numerical set-ups, the reader is referred to deliverable D1.2 (Jüngst, Kaiser, & Geiler, 2017) and the following sections.

1.3 Results

Here the main results obtained in the two considered set-ups are presented.

1.3.1 Constant volume chamber

For the constant volume chamber, a grid sensitivity study is first presented, followed by a comparison between normal gasoline operation and flash-boiling, including both penetration length and spray morphology evolution. Next, the influence of the injection pressure is evaluated for the normal gasoline operation.

1.3.1.1 Grid sensitivity

As a first step, the possibility to relax the grid size toward engine suitable dimensions has been evaluated for OP1, taken as the reference case. Two grid sizes have been evaluated. Each grid has 8 *mm* cells in the far field, and is progressively refined getting closer to the injector nozzle. The coarser grid has cells of 1 mm near the injector, while the finer grid has an additional refinement level leading to 0.5 mm cells near the injector. These grid sizes near the injector may be both well suited for engine simulations, from both accuracy and efficiency point of view. Figure 2 shows the central section of the finer grid on the yz-plane.

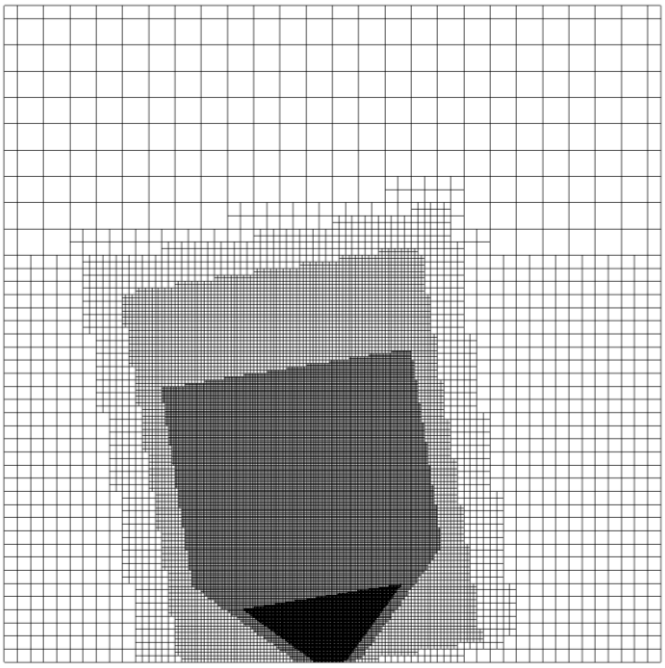

Figure 2: Constant volume spray chamber mesh with finer resolution of 0.5 mm.

Results of spray vapour penetration for the two meshes, computed employing ECN criteria with 0.1% threshold for vapour mass fraction, are shown in Figure 3.

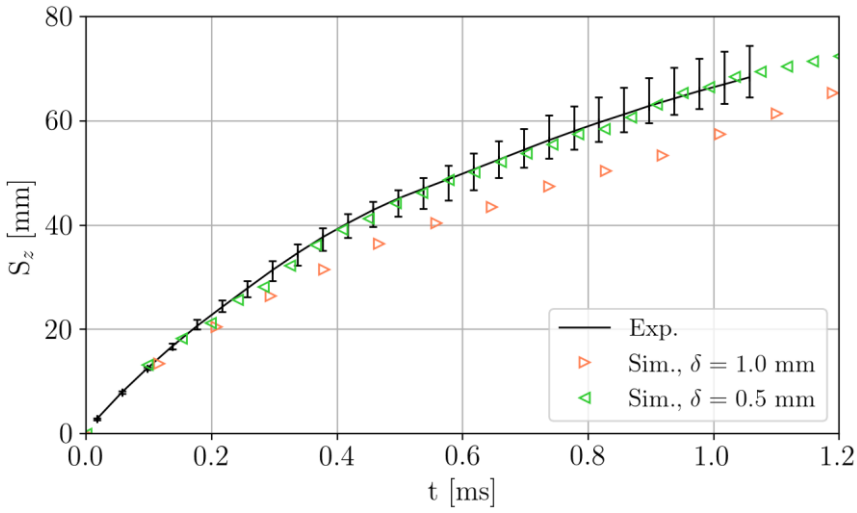

Figure 3: Vapour penetration grid sensitivity study for OP1.

The grid study reveals that in principle both grid sizes may be employed for spray simulations: the grid size with 0.5 mm near the nozzle has been selected here in order to have a better accuracy, and was then tuned in order to match with the experimental conditions. The same parameters were then employed with the coarser gird. Even if this second case deviates from the experimental results, a further tuning appropriate for the coarser grid may be pursued to employ this coarser grid. For the future studies conducted in the optical engine, the finer grid may be already well suited, and it is a good compromise between accuracy and efficiency.

1.3.1.2 Non- and flash-boiling conditions comparison

In this section, results of the spray injection for the non-flash boiling condition first and for the flash-boiling conditions later, are presented. A direct comparison of vapour penetration and liquid penetration of the two cases is also provided. The validation with the experiments of the two cases is performed by comparing both vapour penetration as well as spray morphology evolution from a lateral view of the spray.

1.3.1.2.1 Vapour penetration

In Figure 4, the vapour penetration length is reported for six realizations of OP1, together with their mean and the experimental results.

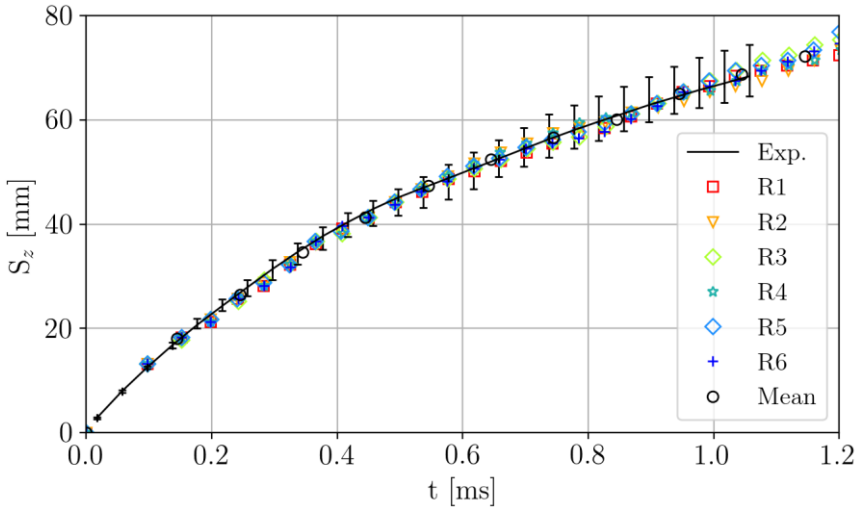

Figure 4: Vapour spray penetration comparison for the six realizations of the simulations, their mean, and the mean of the experimental measurements for OP1.

The figure shows a good comparison between the mean vapour penetration computed in the simulations and the one measured in the experiments at Bosch. Moreover, the figure shows the variability between the six realizations, which is however quite limited, in particular compared to that of the experiments, which is provided by the black error bars showing minimum and maximum of the experiment. It has to be noted, that while in the experiments there might be a slight difference between individual injection events, in the simulation this variability is avoided.

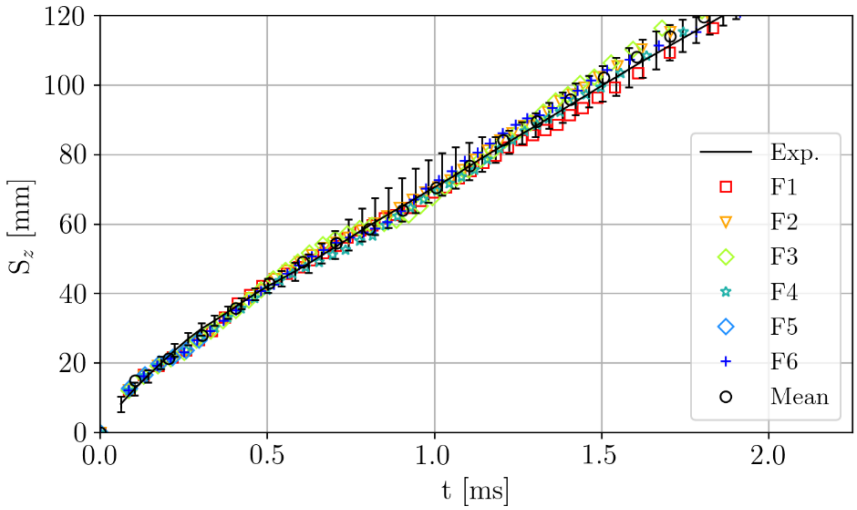

Figure 5: Vapour spray penetration comparison between the six realizations of the simulations, their mean, and the mean of the experimental measurements for OP2.

For the flash-boiling condition OP2, the results are reported in Figure 5, with the same realizations and means as in Figure 4. As before, for this flash-boiling case, the comparison of vapour penetration is excellent, in particular for what concerns the mean of the simulations and the experiments. On the other side, the maximum and the minimum of the experiments are never achieved by the simulations.

A direct comparison of both non- and flashing conditions is shown in Figure 6.

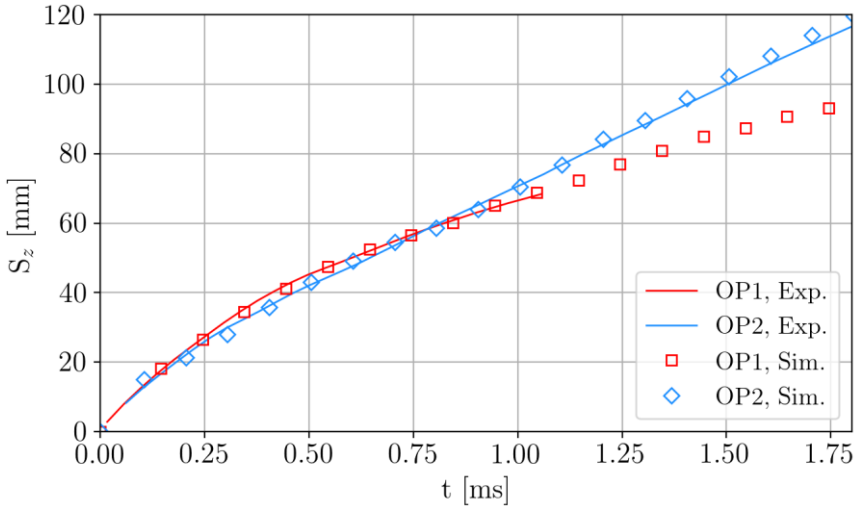

Figure 6: Comparison of non- and flash-boiling vapour penetration length.

The comparison highlights the strongly different dynamics between the two operating conditions OP1 and OP2, where the first case has a slightly higher penetration rate at earlier stages, while at later stages the vapour penetration of the flash-boiling case takes-over and penetrates consistently faster.

1.3.1.2.2 Liquid penetration

In Figure 7, the liquid penetration length for non- and flash-boiling conditions are compared for the cases of the simulations only, since no experimental data was available for validation.

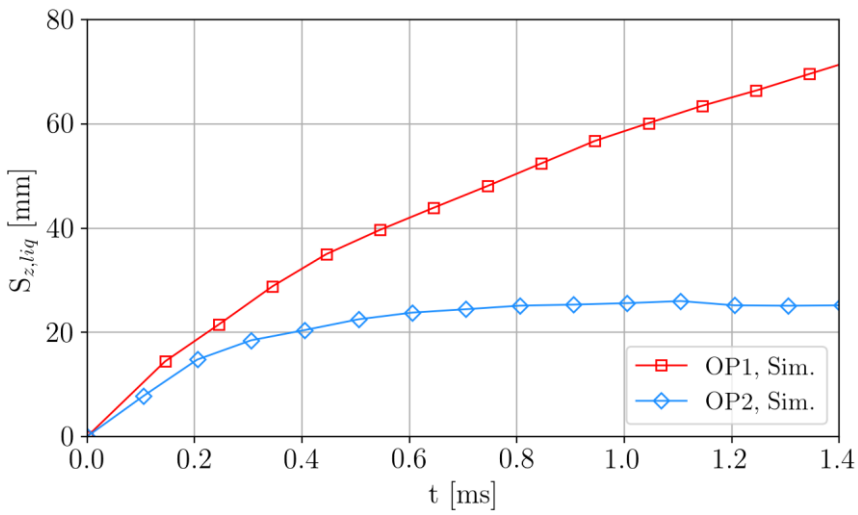

Figure 7: Comparison of non- and flash boiling liquid penetration length.

Contrarily to the vapour penetration, liquid penetration for these two cases is greatly different; in the non-flashing case in fact, liquid penetration reaches much higher values, since some droplets does not evaporate completely. In the flashing case however, the droplets exiting from the nozzle evaporates quite instantaneously and, in fact, the liquid penetration distance saturates at a value of around 25 mm at around 1 millisecond. This, together with the higher vapour penetration rate at later stages, is a strong characteristic of the flashing condition, contrasting the behaviour of the non-flashing condition.

1.3.1.2.3 Spray morphology evolution

To have a deeper understanding of the spray morphology differences between the non-flashing and the flashing conditions with subsequent spray collapse, in Figure 8 snapshots of both experiments and simulation at different subsequent times are reported.

The first line of figures reports results at 0.1 ms, the second at 0.5 ms, the third at 1.0 ms and finally the fourth at 2.0 ms. The first two columns from left, reports non-flashing conditions comparison, while the third and fourth columns the flashing conditions. First and third columns shows shadowed images of spray evolution recorded in the experiments, while second and fourth columns are images of mixture fraction iso-surfaces coloured with velocity magnitude.

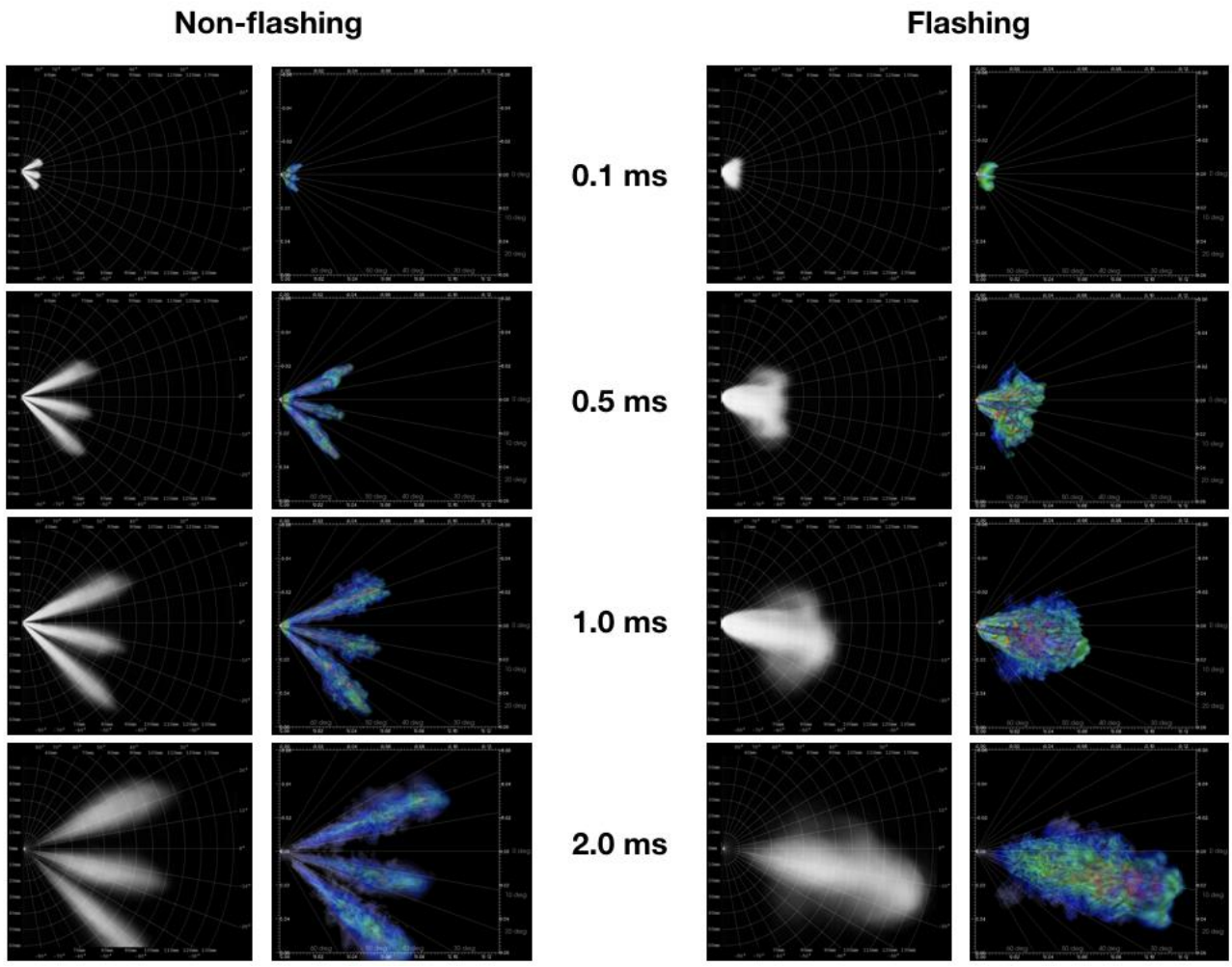

Figure 8: Spray morphology evolution for non-flashing conditions, left two columns, and flashing conditions, right two columns. First and third columns report experimental results while second and fourth columns simulations results.

The series of images shows one major difference in the spray morphology between the different operating conditions: in the non-flashing case, every spray associated with each nozzle can be distinguished by the

others, while in the case of flash-boiling all sprays collapse to form a single jet. This collapse, in turn, together with lower ambient pressure that lower the drag, is the driving mechanism that increase the penetration rate of the spray for OP6.

The simulation of flash-boiling, here, is enabled by the combination of the Reitz-Diwakar model together with the KHRT model. These models, in fact, enable the break-up process appearing at the nozzle exit during flash-boiling to be mimiced, i.e. the formation of a large number of small droplets. At the same time, specification of the semi-cone angle allows the widening of the spray to be adjusted when the ambient pressure is drastically reduced. This leads to a semi-cone angle of around 41° under flash-boiling conditions due to the low ambient pressure, in contrast to the typical 16-17° typical of Diesel and gasoline spray injection at high and normal ambient pressures respectively.

1.3.1.3 Injection pressure influence

In the following sections, injection pressure influence is investigated and the ability of the numerical simulations to predict the behaviour at different injection pressures is evaluated.

1.3.1.3.1 Vapour penetration

In Figure 9, vapour penetration for operating condition OP3 is reported.

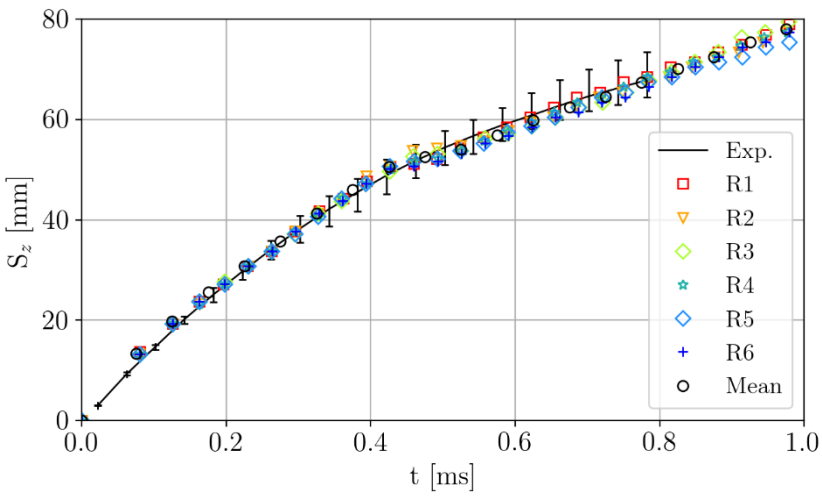

Figure 9: Vapour spray penetration comparison between the six realizations of the simulations, their mean, and the mean of the experiment for OP3.

As for the previous cases, here the penetration length is also very well reproduced by the simulation.

In order to highlight the influence of the injection pressure on the spray vapour penetration, the two penetration lengths obtained in the simulations are reported in Figure 10, together with experimental results. As expected, a higher injection pressure increases spray vapour penetration, since the injected mass as well as the nozzle exit velocities are both higher for the higher injection pressure.

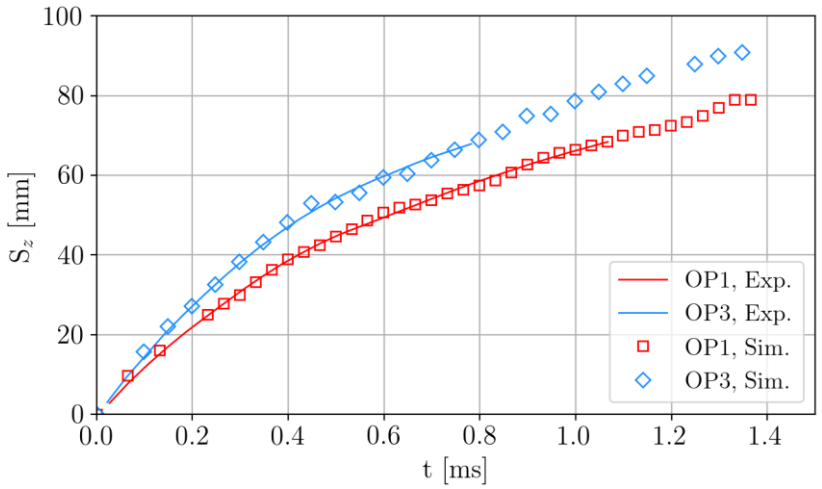

Figure 10: Comparison of non-flash boiling vapour penetration length at two different injection pressures: 20MPa, OP1, and 35 MPa, OP3.

1.3.1.3.2 Liquid penetration

In Figure 11, the liquid penetration length simulated is compared for the two different injection pressures of OP1 and OP3. As for the vapour penetration length, in the case of the liquid penetration a higher injection pressure leads to a higher liquid penetration length, as expected. In practice, this behaviour leads to a higher probability of forming a thicker liquid film at the case of a wall (piston, in the case of internal combustion engines) close to the injector location.

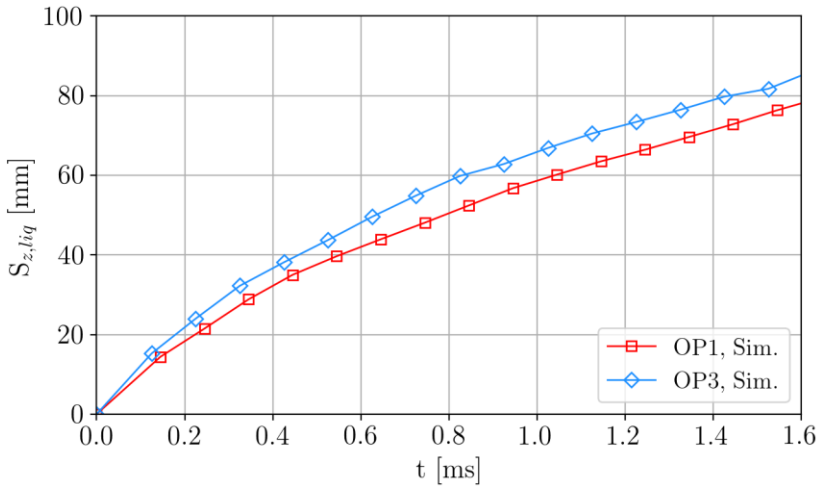

Figure 11: Comparison of non-flash boiling liquid penetration length at two different injection pressures: 20MPa, OP1 and 35 MPa, OP3.

1.3.1.3.3 Spray morphology evolution

Contrary to the comparison of the non- and the flashing condition in Section 1.3.1.3.3, with changes in pressure the morphology of the spray evolves similarly, as shown in Figure 12. The only difference, as anticipated by the vapour penetration comparison, is a slightly higher penetration length, accompanied by a slightly increased spray-cone angle.

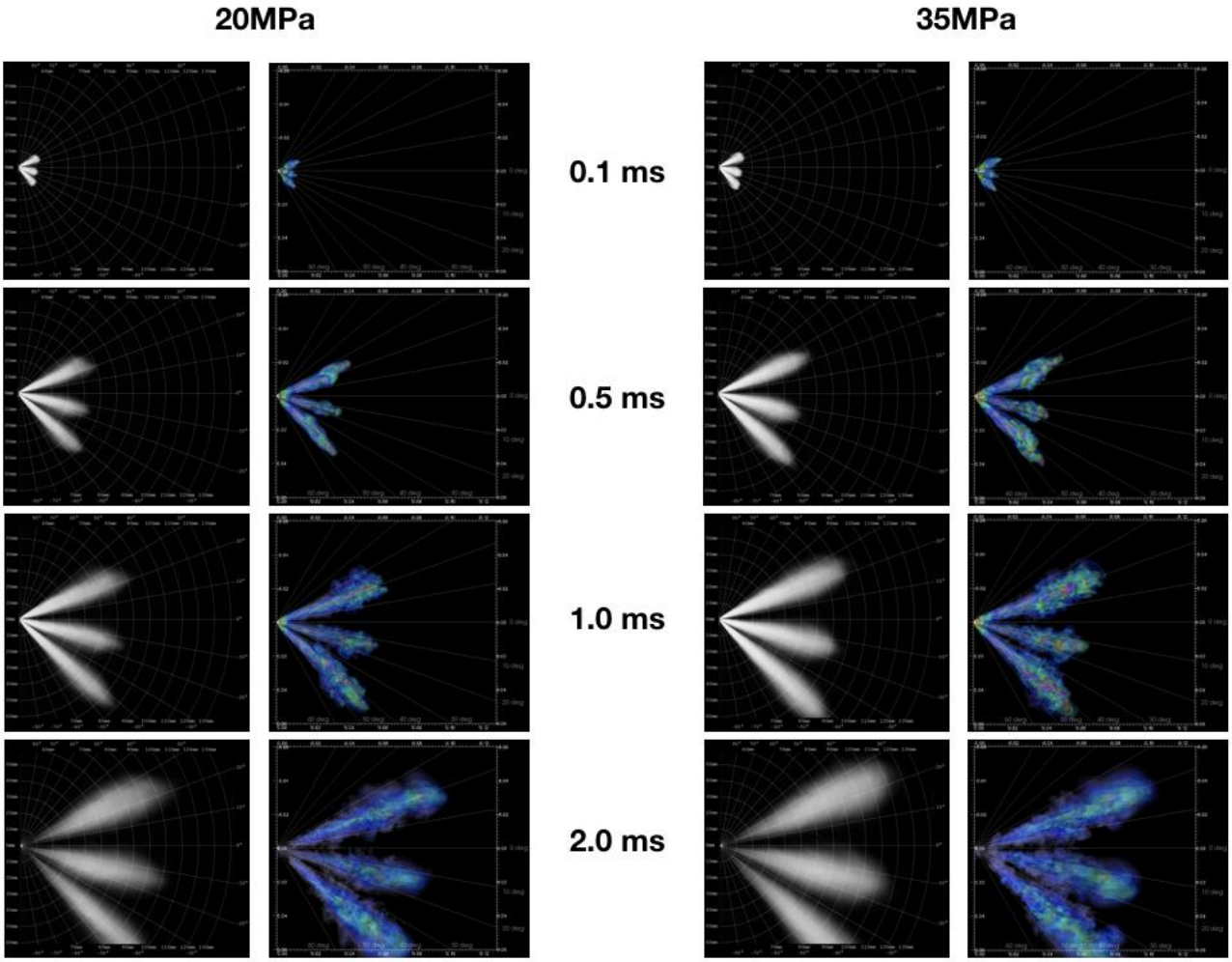

Figure 12: Spray morphology evolution for 20 MPa injection pressure, left two columns, and 35 MPa injection pressure, right two columns. First and third columns report experimental results while second and fourth columns simulations results.

1.3.2 Optical engine

1.3.2.1 Standing piston

Validation of the liquid film is performed first by simulating the fuel injection in the optical engine with a still standing piston. This way, the interaction of complex flows due to the intake and exhaust valve motions is avoided and the film modelling capabilities of Star-CD are more deeply understood.

In order to first evaluate the influence of many parameters playing an important role on the wall film formation and evolution, Figure 13 sketches the evolution of the wall-film mass over time employing different sub-models and tuning parameters. The reference case used is with the piston position P360 and injection pressure 35 MPa, with 10^7 injected parcels per second, a no collision model between droplets, a coverage ratio of $\gamma_c = 0.1$, evaporation without condensation, and a Bai model coefficient A_w of 1320. The wall temperature, T_{wall} was set to 20° C the Bai regime relevant to present simulations is the first of Section 1.1.2.6.

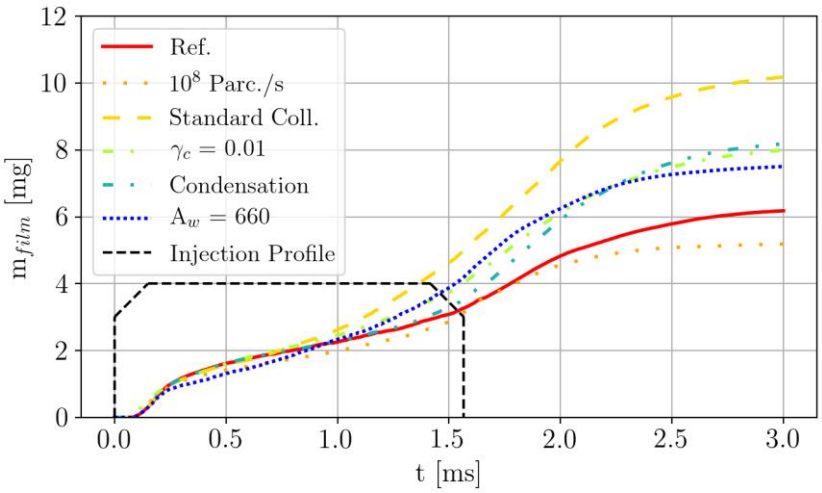

Figure 13: Wall-film mass evolution for different wall-film sub-models and tuning.

The plot shows that, independently of the sub-model or tuning parameter, the general wall-film mass behaviour is the following: initially, after a certain lag between start of injection and the moment the first droplets reaches the piston face, obviously no wall-film mass is present. After this lag, the wall-film starts to form and the first droplets sticks to the wall, leading to a fast growth of the wall-film mass. After this initial phase, the wall-film has formed and the droplets arriving in the wall-film region simply add additional mass to the liquid film already present on the piston. In this phase, as shown in Figure 13 after 0.4 to 0.5 milliseconds, the wall-film mass increases nearly linearly and continuously. After this linear phase, an increase of the rate of mass is observed, mainly due to the end of injection, where the last amount of fuel is not completely evaporated due to the lower injection velocity of the final injection phase: the lower the injection velocity, the lower the drag, and then the lower the evaporation, leading to bigger droplets reaching the wall film increasing the wall-film mass formation. After this phase, where the last droplets are reaching the wall, the rate of wall-film mass decreases until a nearly stationary wall film mass is reached.

The trends observed for the different sub-models and tuning parameters also reveal how the wall-film mass (and the wall film shape, not shown here) can be more or less modified. First, it can be seen that increasing the number of injected particles from 10^7 to 10^8 only slightly modifies the wall-film mass evolution; on the other side, such an increase leads to a quite important slowdown of the simulations, thus will be avoided for future simulations. Second, the figure shows also that taking into account collision among droplet, other than being more realistic for condensed sprays, also leads to a much higher wall-film mass formation, and thus will be considered in present simulations, as for the case of the constant volume spray set-up. By decreasing the surface coverage ratio from 0.1 to 0.01, the wall film mass increases considerably; this is mainly due to the fact that decreasing this parameter leads to a more extended wall-film more quickly, so that there is more time for the next droplets reaching the piston to merge with the already existing wall-film leading to a faster increase. In the present simulations, a surface coverage ratio of $\gamma_c = 0.01$ will be employed. The same effect can be reproduced by including condensation in the wall-film formation process. Including condensation in fact, may produce formation of wall-film from the vapour reaching the piston region. This process leads to a faster wall film formation, so that following droplets contributes quickly to increase the wall-film mass by sticking on the already existing wall-film. Condensation is, therefore, included in the present simulations. Finally, the plot also shows that by decreasing the Bai model coefficient A_w from 1320 to 660 increases considerably the wall-film mass formation.

In the following, simulations at three different piston positions, P360, P330 and P300, are presented for an injection pressure of 35 MPa.

1.3.2.1.1 Piston position variation at 35 MPa injection pressure

In Figure 14, an overview over the wall-film formation at the three piston positions considered here is provided for an injection pressure of 35 MPa.

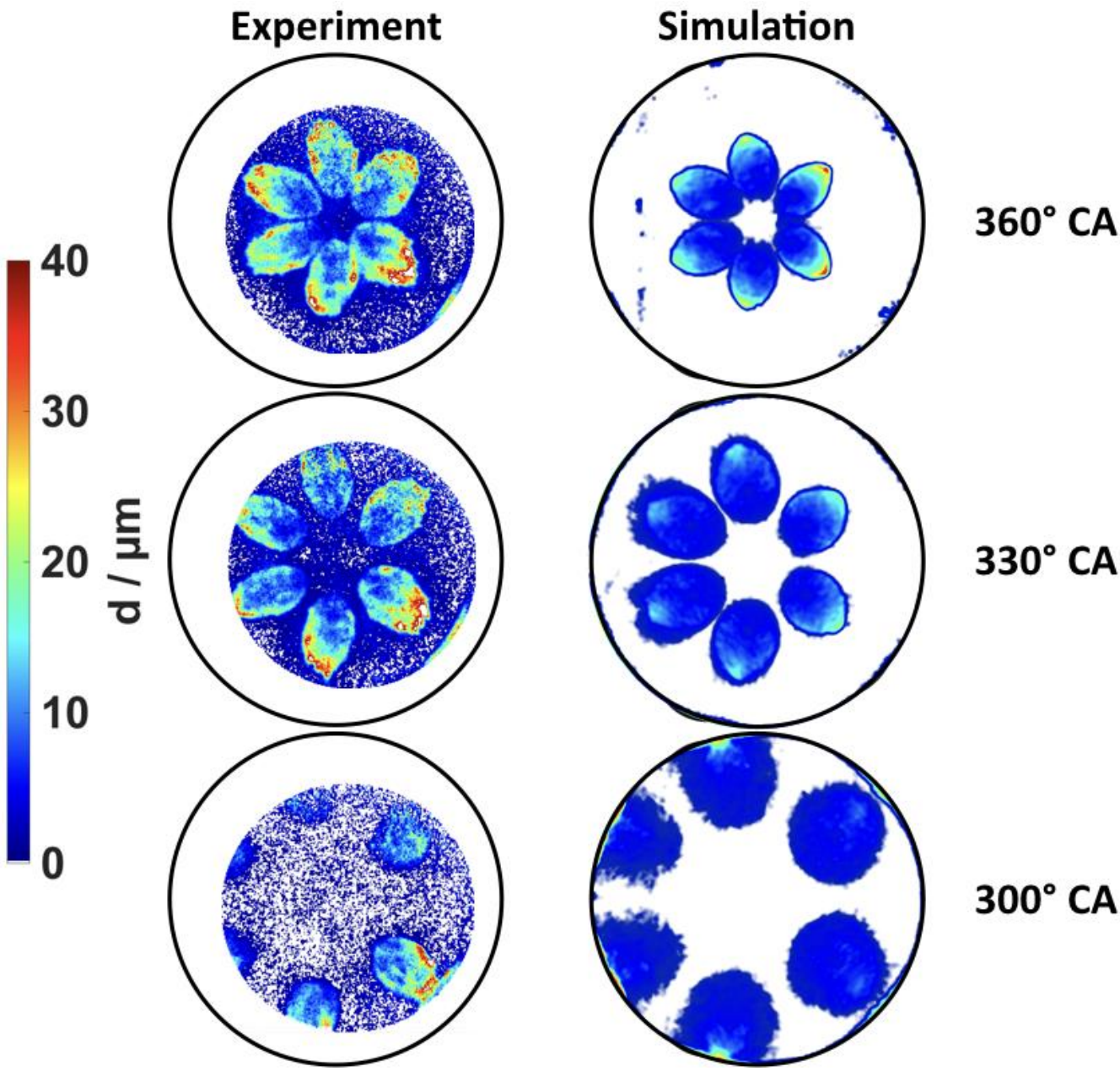

Figure 14: Comparison between experimental measurement (left column) and simulations (right column) of wall-film thickness for different standing piston positions for injection pressure 35 MPa.

Starting from the piston position P360, good comparisons can be observed in both the wall-film thickness and the shape. Wall-film thickness in fact compares quantitatively good at the "tip" of the liquid film "fingerprint", reaching nearly a thickness of 40 µm, and then decreases progressively towards the centre of the piston. Comparison of the shape is also quite good, both with respect to the orientation of the wall-film fingerprint, which changes depending on the position of the spray nozzle due to injector tilting, as well as with respect to the changing of the extension, which increase for the fingerprints toward the left-hand side.

By changing the piston position to P330, the liquid-film footprint moves progressively toward the cylinder wall. This is also well reproduced by the simulations. On the other hand, the wall-film thickness toward the liquid film "tip" is slightly underestimated by the simulations. By further lowering the piston position, a similar trend can be observed: progressive motion of the liquid film towards the piston and wall, and decrease of the wall-film thickness, which also for this case is slightly underestimated by the simulation.

In Figure 15, the total mass of the wall-film as a function of time is reported, for the entire duration of the simulation, and for all three piston positions and injection pressure of 35 MPa. In the inset of the same figure, the same quantities are reported with a focus in the time range between 0 and 2 ms.

At around 10 ms, the wall-film mass evolution is nearly constant, thanks to the favourable condition of ambient temperature and walls at 20° C in both experiments and simulations, so that at this stage the liquid film solution as reported for simulations in Figure 14 can be compared to the liquid film measured at 180 ms, also reported as a comparison in Figure 14.

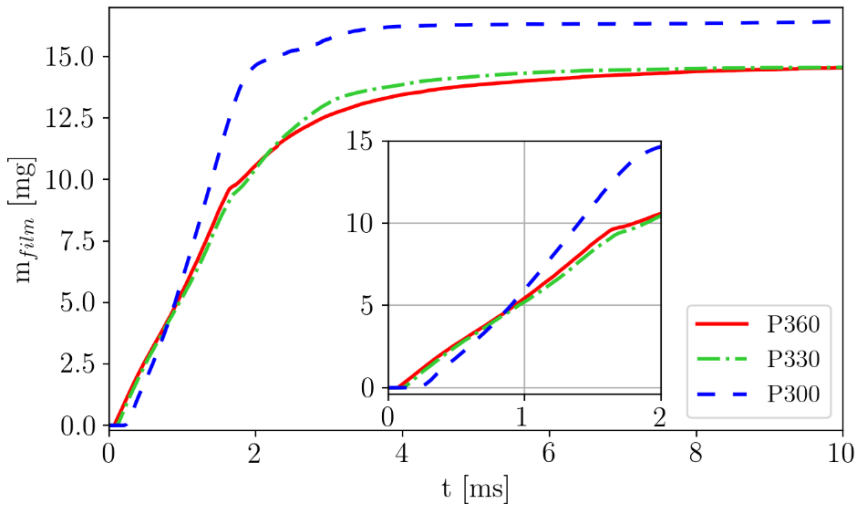

Figure 15: Wall-film mass evolution for injection pressure 35 MPa at three different positions: P360, P330 and P300.

Two main influences of the different piston positions can be noted in the inset of Figure 15: a delayed wall-film formation with decreasing crank-angle, and an increased wall-film mass for the piston position P300. The delayed wall-film formation is simply explained by the longer axial distance the droplets need to travel in order to reach the piston with lowering crank angle. The increased wall-film mass formation for the piston position of P300 is perhaps due to the increased cross-sectional area covered by the spray cone at piston location, leading to a more extended fingerprint since the early stages of the injection. A wider fingerprint and a higher wetted area lead, in turn, to an enhanced deposition rate of the droplets, also shown by the steeper mass flow deposition of the P300 run with respect to the other two positions, between 0.25 and 1.7 ms.

1.3.2.1.2 Piston position variation at 20 MPa injection

As in Figure 14, in Figure 16 an overview over the wall-film formation at the three piston positions considered here is provided but for an injection pressure of 20 MPa.

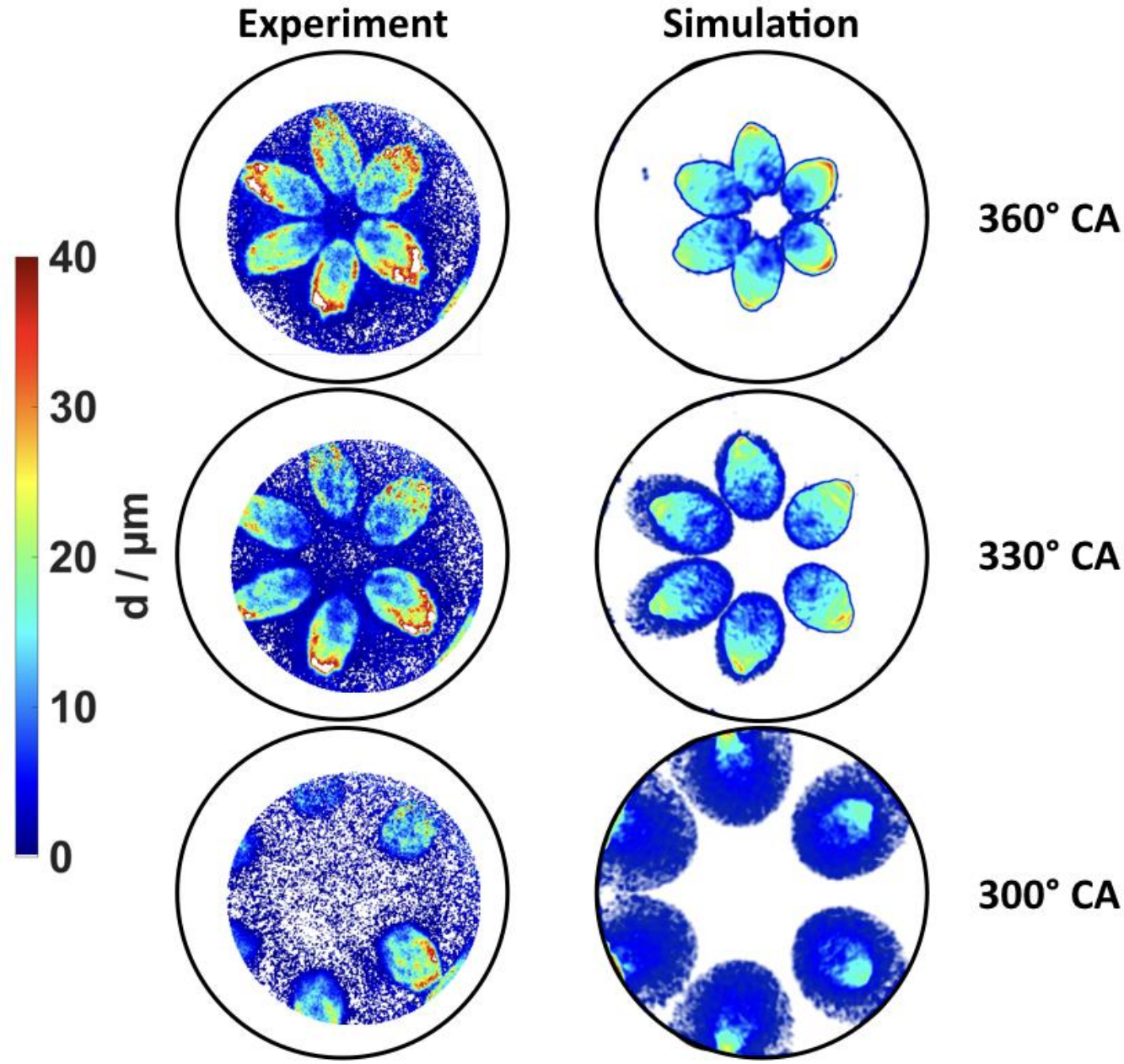

Figure 16: Comparison between experimental measurement (left column) and simulations (right column) of wall-film thickness for different standing piston positions for injection pressure 20 MPa.

Also in this case, the trends are well captured: as the piston moves away from the injector, the spray foot print forming the liquid film moves toward the cylinder walls. Moreover, direction and extension of the wall-film "plumes" are also similar to the experimental measurements. Finally, the liquid film is also nearly quantitatively captured, even if for these cases the mismatch with the experiments is higher than for the cases with injection pressure 35 MPa.

2 Discussion and Conclusions

The present report deals with the assessment and validation of the numerical simulations of the constant volume spray chamber and optical engine within the PaREGEn project framework. Both measurements and simulations aim to provide insights into the Cause and Effect Relationship (CER) of soot formation in gasoline direct injection engines. The first step toward deeper understanding on the CER behind soot formation is to have a good understanding of the spray formation and development together with the subsequent formation of wall-film depending on the operating conditions.

Spray formation and development was investigated, in the measurements, by shadow images, from which the vapour penetration length is extracted, and is used as main quantitative result to validate the simulations. Shadow images allow also to compare spray shape and morphology evolution, which is an effective way of validating numerical simulations, in particular in order to investigate if the model is able to reproduce important characteristics of the operating condition. This was the case when investigating the capability of the numerical model to reproduce both standard gasoline injection operating conditions at ambient pressure (1 bar), but also gasoline injection under flash-boiling conditions, leading to spray collapse. In this report, it is shown that the models and sub-models employed here are able to capture very well both the spray vapour penetration length and the spray morphology evolution in both cases. For the non-flashing conditions, injection pressure effects were also investigated. In this case as well, the model is able to reproduce very well both vapour penetration and spray morphology evolution.

With the validated spray model, simulations of wall-film formations have been carried out. As a first step towards the wall-film and the sub-models' validation, the optical engine with standing piston is considered; this avoids the complex flows related to piston motion together with intake and exhaust valve opening and closing. Thus, the spray, already validated in the constant volume chamber, can be directly transferred to a different geometry, where attention can be focused on the wall-film formation. It was shown here that the wall-film simulation performed well for varying piston positions when the injection pressure was set to 35 MPa. In this case, the liquid film thickness can be predicted quantitatively, while the liquid film morphology is very similar to the one measured in the experiments. When the injection pressure is decreased to 20 MPa, the simulations compares less well than those with an injection pressure of 35 MPa. However, it has to be noted that, for all the six simulations, the tuning parameters related to the droplet/wall interaction and wall-film modelling are kept the same and are not adapted to each condition. This renders the model more general, and confirms that overall the combination of models and sub-models presented here provides a very good prediction capability for spray development and spray/wall interaction simulations.

Building on these wall-film simulations in the optical engine with stationary piston, moving piston data will be used in a next step for further validation. In this case, the interaction of the complex bulk flow motions due to intake and exhaust processes, producing significant levels of turbulence, will be taken into account in order to obtain more realistic conditions towards real engines applications. At the same time, simulations of wall-film in the flow channel will be performed in parallel to the optical engine with moving piston. Both cases will be then employed to further increase the complexity of the simulations by including combustion and, furthermore, soot formation. In these cases, wall-film formation and evaporation will play a very important role for the formation of soot under reacting conditions.

The work performed until now, investigating the potential for numerical simulations to reproduce spray and spray/wall interactions, constitutes an excellent basis for further development towards ever more complex phenomena appearing in gasoline direct injection engines, where accurate prediction of the mixture formation is fundamental in order to model, with a high degree of fidelity, the combustion processes and subsequent emissions.

3 Deviations and Risks

3.1 Deviations

3.1.1 Description of work related to deliverable in GA Annex 1 – Part A

The objectives of the present deliverable were set by following a bottom-up approach: first, spray models are calibrated using data obtained in the constant volume chamber at Bosch. Next mixture formation and spray/wall interaction models are assessed in the flow channel, allowing to further extend the simulations toward reacting flows. Finally, the wall-film formation arising from the spray/wall interaction and the respective numerical models and sub-models employed to simulate it are assessed in the optically accessible engine at Bosch. The results reported here, in general, cover the overall objectives of the present deliverable: first, mixture formation and spray development have been calibrated and then validated by both vapour penetration length and spray shadow images for three different operating conditions, covering non-flashing and flashing conditions, reaching then the set objectives. Next, spray/wall interaction simulations with subsequent liquid-film formation has been reported, for two different injection pressures and three different fixed piston positions.
Additional operating conditions allowing for further, in-depth validation of the developed framework will be simulated in the near future, using the same geometry and operating conditions but with motored conditions and moving piston. Finally, the still on-going flow channel experiments using the designated project injector did not allow for further comparisons using this alternative configuration yet. Simulations of this set-up will be conducted soon, and rapidly extended also to reacting conditions, before engaging in reactive engine calculations foreseen in the remainder of this subtask.

3.1.2 Time deviations from original planning in GA Annex 1 – Part A

There are no deviations with respect to timing of this deliverable

3.1.3 Content deviations from original plan in GA Annex 1 – Part A

There is no significant deviation in terms of content.

3.2 Risk Register

Risk No.	What is the risk	Probability of risk occurrence[1]	Effect of risk[2]	Solutions to overcome the risk
1	Section 2.1.2: Employment of Lagrangian model for the liquid phase of the spray may decrease accuracy when simulating operating points outside the validated ones.	2	2	Execute, if possible, a validation of the spray for the given operating condition before moving to more complicated configurations.
2	Sections 2.1.2.6 and 2.1.3: droplet/wall interaction models and wall-film models employs a large number of empirical parameters which may affect considerably the simulations when simulating operating points outside the validated ones.	2	2	Execute, if possible, a validation of the wall-film for the given operating condition before moving to further complicated simulations.

[1] Probability risk will occur: 1 = high, 2 = medium, 3 = Low

[2] Effect when risk occurs: 1 = high, 2 = medium, 3 = Low

3	Section 2.3.11: the finer mesh with smaller cells of 0.5 mm may be too expensive for engine simulations including combustion and detailed chemistry.	1	2	Repeat the tuning of the most important parameters of spray and wall-film modelling in order to match the simulations with experimental data.

4 References

[1] E. Sher, T. Bar-Kohany and A. Rashkovan, «Flash-boiling atomization,» *Progress in Energy and Combustion Science,* vol. 34, p. 417–439, 2008.

[2] M. Germano, «Turbulence: the filtering approach,» *J. Fluid Mech.,* vol. 238, n. 1, pp. 325-336, 1992.

[3] K. Horiuti, «A proper velocity scale for modelling subgrid-scale eddy viscosities in large eddy simulation,» *Phys. Fluids A,* vol. 5, pp. 146-157, 1992.

[4] Siemens PLM Software, «STAR-CD Methodology v4.28,» 2017.

[5] F. Bracco, «Modeling of engine sprays,» *SAE Technical Paper Series,* vol. 850394, 1985.

[6] F. Obermeier, «Modeling of nozzle-flow,» *IDEAProject, Subprogram A1,* 1991.

[7] R. Reitz and R. Diwakar, «Effect of drop breakup on fuel sprays,» *SAE Technical Paper Series,* n. 860469, 1986.

[8] M. Patterson and R. Reitz, «Modeling the effects of fuel spray characteristics on Diesel engine combustion and emission,» *SAE Paper Series,* n. 980131, 1998.

[9] P. O'Rourke, «Collective drop effects on vaporising liquid sprays,» University of Princeton, 1981.

[10] C. Bai and A. Gosman, «Development of methodology for spray impingement simulation,» *SAE Technical Paper Series,* n. 950283, 1995.

[11] C. Bai and A. Gosman, «Mathematical modeling of wall films formed by impinging sprays,» *SAE Technical Paper Series,* n. 960626, 1996.

[12] W. Sirignano, «Fluid Dynamics and Transport of Droplets and Sprays,» *Cambridge University Press,* 1999.

[13] D. Torres, P. O'Rourke and A. Amsden, «Efficient multicomponent fuel algorithm,» *Combust. Theory Modelling,* n. 7, p. 67, 2003.

[14] N. Jüngst, S. Kaiser and J. Geiler, «Deliverable D1.2: Report on basic set of results from spray and fuel-film imaging in the optical engine for preliminary validation of corresponding 3D LES simulations,» 2017.

Appendix A – Acknowledgement

The authors would like to thank the partners in the project for their valuable comments on previous drafts and for performing the review.

Project partners:

#	Partner	Partner Full Name
1	RIC	RICARDO UK LIMITED
2	DAI	DAIMLER AG
3	JLR	JAGUAR LAND ROVER LIMITED
4	BOSCH	ROBERT BOSCH GMBH
5	FEV	FEV EUROPE GMBH
6	JM	JOHNSON MATTHEY PLC
7	HON	HONEYWELL, SPOL. S.R.O.
8	JRC	JOINT RESEARCH CENTRE – EUROPEAN COMMISSION
9	UNR	UNIRESEARCH BV
10	IDIADA	IDIADA AUTOMOTIVE TECHNOLOGY SA
11	SIEMENS	SIEMENS INDUSTRY SOFTWARE SAS
12	LOGE	LUND COMBUSTION ENGINEERING LOGE AB
13	ETH	EIDGENOESSISCHE TECHNISCHE HOCHSCHULE ZUERICH
14	UDE	UNIVERSITAET DUISBURG-ESSEN
15	RWTH	RWTH AACHEN UNIVERSITY
16	UFI	UFI FILTERS SPA
17	UOB	UNIVERSITY OF BRIGHTON
18	GARR	GARRETT–ADVANCING MOTION

This project has received funding from the European Union's Horizon2020 research and innovation programme under Grant Agreement no. 723954.